Electronic stopping of iron for protons and helium ions from first-principles calculations

Xu-Dong Zhao [1], Fei Mao [2,*] and Huiqiu Deng [1,3,†]

[1] *School of Physics and Electronics, Hunan University, Changsha 410082, China*

[2] *School of Nuclear Science and Technology, University of South China, Hengyang 421001, China*

[3] *College of Materials Science and Engineering, Hunan University, Changsha 410082, China*

(Received 30 July 2023; revised 10 January 2024; accepted 13 February 2024; published 11 March 2024)

The electronic stopping power and charge state of protons and helium ions irradiating iron under both channeling and off-channeling geometries are studied by first-principles molecular dynamics. Using real-time time-dependent density functional theory, the inner-electron excitation of iron under ion irradiation is explored. The calculated electronic stopping powers, which take into account the effects of inner-electron excitation, were found to be in good agreement with experimental data. To further investigate the charges attracted by the projectiles moving in iron, we introduced a modified method to decompose the charges into the occupations of the respective projectile orbitals. When the projectile ion moves along off-channeling trajectories, the orbital distribution of the charges attracted by protons is found to be unstable, while that of helium ions remains relatively stable. However, it is worth noting that the orbital distribution differs between the channeling and off-channeling cases for both protons and helium ions. Overall, our research provides insight into the electron capture behavior of protons and helium ions as they traverse through iron.

DOI: 10.1103/PhysRevA.109.032807

I. INTRODUCTION

The interaction between energetic ions and matter has been an object of great interest since the last century [1]. As a fundamental physics research topic, its advancement has abundant implications for nuclear materials related to fusion-fission reactors [2–4], ion beam irradiation-based cancer therapy [5–7], materials engineering for aerospace activities [8–10], etc. The energetic ions continuously deposit kinetic energy as they travel in materials. There are two main channels for the target material to gather kinetic energy of the projectile ions: elastic collision with target nuclei and inelastic energy loss due to electron excitation. The stopping power S [the kinetic energy loss dE of the projectile per penetration depth dx ($S = -dE/dx$)] is proposed to measure this energy deposition quantitatively [11,12]. According to the mediums of energy depositions, one can divide the stopping power S into the nuclear stopping power S_n and the electronic stopping power S_e.

At lower ion velocities, S_n contributes significantly to the energy deposition, which predominantly generates lattice displacement. However, S_e is also substantial via the excitation of the outer electrons, which exhibits a particularly complex behavior due to the electronic structure of the projectile-target combination. The S_e of metals for light ions, such as protons and helium ions, is proportional to the velocity of the ions in the low-velocity regime. For example, the S_e of protons in Al [13,14] is explained by the free electron gas (FEG) model [15,16]. For transition metals, such as Cu, Zn, Au, Ag, and Pt [13,17–20], the S_e exhibits pronounced deviations from velocity proportionality, generally considering it caused by the finite excitation threshold of d electrons. Meanwhile, this deviation disappears for d-electron-poor transition metals, such as Ti, Gd, and Ta [21,22]. Therefore, it is a fascinating physical question of how the S_e of transition metals with a half-filled d band behave, and this study can lead us to achieve a deeper understanding of the deviation from the velocity proportionality of S_e.

At higher ion velocities, the projectile ions lose most of the kinetic energy by electronic stopping, and the inner electron excitation provides additional channels for energy loss. In this velocity regime, although light ions provide only a weak perturbation to the target atomic electrons and the first-order perturbation theoretical models [23–25] can describe the electronic energy loss precisely, it is still attractive to investigate which inner-shell electrons are involved in the electronic energy loss [26]. For example, for the $2s$ and $2p$ electrons of Si [27] and Al [28], the $3p$ electrons of Ni [29], and the $1s$ electrons of H_2O [30], etc., these results showed that inner electrons offer non-negligible improvements in the electron dynamics.

Another quantity of great interest is the charge state of the projectiles interacting with solids. When an energetic ion travels through materials in simulations, it is hard to separate the charges captured by the ion from the materials, and one can only artificially define a boundary. Even if an incident ion has escaped from the materials, it is accompanied by bound electrons. Recently, Kononov *et al.* [31] proposed a method that uses the radial distribution of isolated hydrogen atomic orbitals to linearly fit the radial distribution of the charges captured by protons after the proton escapes from an aluminum target, thus decomposing the charges captured by protons into

*Corresponding author: maofei@mail.bnu.edu.cn

†Corresponding author: hqdeng@hnu.edu.cn

the occupations of hydrogen orbitals. This treatment opens a different way to understand the fundamental physics of charge capture.

In this article, we performed electron-ion dynamics simulation of protons and helium ions irradiating Fe and focus on three issues: first, to explore the velocity proportionality of the S_e in the low-velocity regime; second, to investigate the contribution of the inner-electron excitation to the S_e; and third, to obtain the orbital distribution of electrons captured by the projectiles traveling in Fe for both channeling and off-channeling trajectories.

II. METHOD AND COMPUTATIONAL DETAILS

In this work, real-time time-dependent density functional theory (RT-TDDFT) [32–34] coupled with Ehrenfest molecular dynamics as implemented in the real-space code OCTOPUS [35,36] was used to simulate electron-ion dynamics of protons and helium ions traversing in bulk Fe. A supercell including 108 Fe atoms is constructed from $3 \times 3 \times 6$ conventional cubic cells, which was chosen to minimize the spurious effects of the repetitions while keeping manageable computational demands for a long off-channeling projectile trajectory. Three-dimensional periodic boundary conditions were used throughout in our simulations. A single k point (Γ) was used for sampling in the Brillouin zone.

The norm-conserving Troullier-Martins pseudopotential [37] was used to describe the interaction between the electrons and the ionic system for both projectiles and host atoms in this simulation. Three pseudopotentials, named Fe8 ([Ar]$3d^6 4s^2$), Fe14 ([Ne$3s^2$]$3p^6 3d^6 4s^2$), and Fe16 ([Ne]$3s^2 3p^6 3d^6 4s^2$), were generated to investigate the inner-electron excitation in the slowing down of the projectiles. The local-density approximation (LDA) with Perdew-Wang analytic representation [38] was employed for the exchange-correlation potential. The external potential, electron density, and Kohn-Sham orbitals are discretized in a set of mesh grid points with uniform spacing of 0.16 Å, corresponding to a grid cutoff of 107 Ry, along all three spatial coordinates in real space in the simulation cell. The initial ground-state Kohn-Sham orbitals are set up by diagonalization of the time-independent Kohn-Sham Hamiltonian for Fe, and the initial wave functions are constructed by the linear combination of atomic orbitals method.

After obtaining the ground-state Kohn-Sham orbitals, an ion is added to the simulated box and given a velocity with a defined direction. The Kohn-Sham orbitals are propagated according to the time-dependent Kohn-Sham equation using the approximated enforced time-reversal symmetry (AETRS) method [39]. The propagation step length $\Delta t \times v \sim 1.44 \times 10^{-3}$ Å is adopted for various velocities to ensure the energy convergence of time-dependent evolution. The target atoms fail to respond to the forces they experienced in time under the femtosecond timescale simulations of the RT-TDDFT, so the host atoms are fixed at their equilibrium positions and do not move while the projectile is in motion. We adopted the method proposed by Schleife *et al.* to extract the off-channeling S_e, as described in Ref. [28], by replacing the average of multiple off-channeling trajectories with a long one; more details can be seen in Fig. S1 of the Supplemental Material [40]. We used a velocity direction [0.444, 0.513, 0.735] (given normalized here) for all the off-channeling simulations.

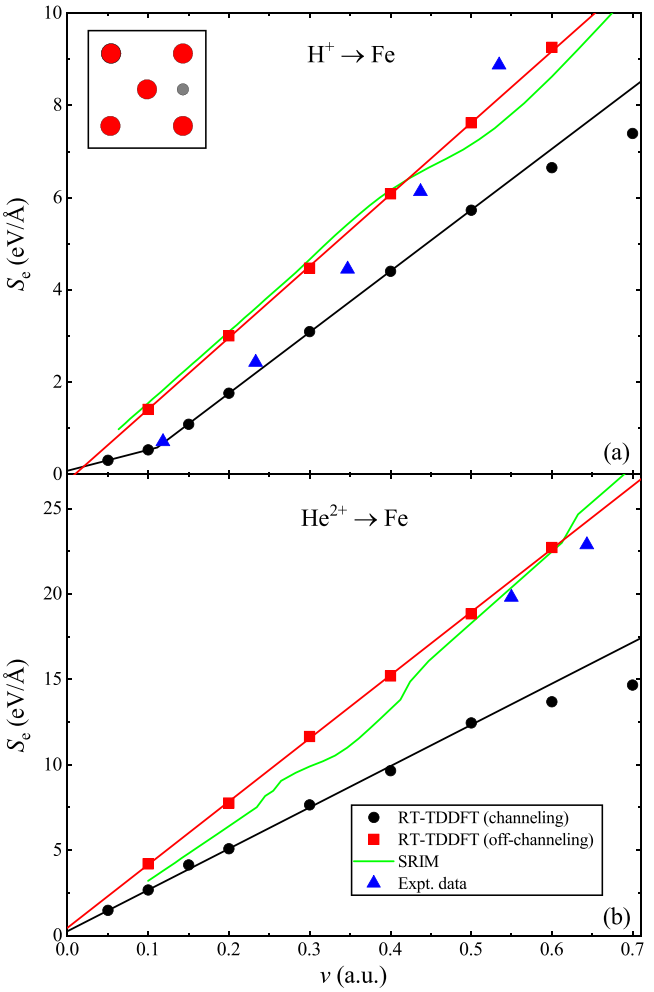

FIG. 1. The S_e of (a) protons and (b) helium ions in Fe in the low-velocity range. The inset in (a) indicates the incidence geometry of channeling projectiles, the red circles indicate Fe atoms, and the gray circle suggests the projectile ion. The blue triangles refer to the experimental database from International Atomic Energy Agency (IAEA) [41] and the green curves refer to the SRIM [42]. The black circles and red squares indicate the simulated results from channeling and off-channeling trajectories, respectively. The black and red lines indicate the linear fit of the channeling and off-channeling results, respectively.

III. RESULTS AND DISCUSSION

A. The channeling stopping

In the low-velocity regime, the contribution of inner electrons to the electronic stopping power is minimal when the projectiles are channeling in Fe. Meanwhile, the pseudopotential radii of projectiles and host atoms are avoided to overlap throughout the whole journey of projectiles, yielding more accurate results. Figure 1 illustrates the RT-TDDFT calculated S_e for protons and helium ions moving in Fe along the [001] crystal orientation within a velocity range of 0.05 to 0.7 a.u. The incidence position is shown in the inset of

Fig. 1(a), which is also referred to as hyperchanneling due to its high-symmetry channel. Additionally, Fig. 1 includes the RT-TDDFT off-channeling S_e, experimental data [41], and the stopping and range of ions in matter (SRIM) predictions [42]. For all the RT-TDDFT simulations in Fig. 1, the Fe14 pseudopotential was employed. The results of calculation of S_e for channeled protons and helium ions are shown in Fig. S2 of the Supplemental Material [40].

As shown in Fig. 1(a), the S_e exhibits two types of behavior: First, the experimental data and calculated channeling S_e display two velocity-proportional slopes on both sides of 0.1 a.u., which is commonly referred to as the kink velocity. This phenomenon can be explained by the fact that only the s-band electrons near the Fermi energy are excited at lower velocities, while the deeper d-band electrons are excited at higher velocities. The excitation of these deeper electrons provides an additional channel for electronic energy loss [12]; Second, the calculated off-channeling S_e and SRIM predictions show a linear velocity dependence. At higher velocities, the off-channeling S_e values agree quantitatively with the experimental data. The difference between the channeling S_e and experimental data decreases as the proton velocity decreases. The channeling S_e aligns well with the experimental data at 0.1 a.u. and is about 30% lower than the experiment at 0.5 a.u. It is worth noting that the kink velocity disappears as the impact parameter of the channeling proton decreases, as shown in Fig. S3 of the Supplemental Material [40]. The decrease in impact parameter directly affects the excitation of deep-lying electrons, suggesting a connection between the kink velocity and the excitation of these deep-lying electrons.

In contrast to protons, the behavior of helium ions shows that both the channeling and off-channeling S_e are proportional to the velocity, as depicted in Fig. 1(b). The off-channeling S_e values agree well with the reference values, while the channeling S_e is underestimated by approximately 30% at a velocity of nearly 0.5 a.u. For d-electron-rich transition metals, such as Cu, Zn, and Ag [17,18], the S_e for both protons and helium ions exhibits deviations from the velocity-proportional trend, but for d-electron-poor transition metals, such as Ti, Gd, and Ta [21,22], the S_e for both protons and helium ions does not exhibit this deviation. However, for the transition metal Fe, the d band is approximately half filled with six d electrons per atom, and the S_e of protons exhibits the aforementioned deviation, while that of helium ions does not.

One of the notable characteristics of the RT-TDDFT is its ability to account for band structure effects in calculations. We examined the distribution of the d band for transition metals with different electronic configurations. As shown in Fig. S4 of the Supplemental Material [40], filled by a few electrons, the d band distributes mainly around the Fermi energy as a conduction band. For the transition metals with a fully filled d band, the d band is highly localized with a band offset, such that a minimum energy is required to excite electrons from the d band. Furthermore, for transition metals such as Fe with a half-filled d band, the d band comprises a few distinct peaks. To investigate the effects of the band structure of Fe on electron excitation for protons and helium ions in the low-velocity regime, the energy distribution of excited electrons and holes is computed. By projecting the time-evolved Kohn-Sham states $\psi_j(t)$ at the final step of the TDDFT simulation onto the Kohn-Sham eigenstates φ_i of Fe, the occupations $n_{\rm occ}(\varepsilon_i)$ in the ih Kohn-Sham state with the ground-state eigenenergy ε_i are obtained,

$$n_{\rm occ}(\varepsilon_i) = \sum_j f_j |\langle \varphi_i | \psi_j(t) \rangle|^2, \tag{1}$$

where f_j are the fixed occupation of the time-evolved Kohn-Sham states $\psi_j(t)$. The populations of holes and excited electrons, $P(\varepsilon_i)$, are obtained as follows:

$$P(\varepsilon_i) = n_{\rm occ}(\varepsilon_i) - f_i, \tag{2}$$

where f_i are the fixed occupation of the Kohn-Sham eigenstates φ_i. The negative and positive values of $P(\varepsilon_i)$ represent the occupations of electron holes and excited electrons, respectively. Summation over all electron holes yields the total number of excited electrons N,

$$N = \sum_{\varepsilon_i < E_F} |P(\varepsilon_i)|. \tag{3}$$

Here, N is proportional to the time t spent by the ions moving through Fe at a given velocity. Because, in our simulation, the projectile is suddenly introduced into the material as a bare ion at $t = 0$, it undergoes a charge capture process when entering the material. Therefore, the $P(\varepsilon)$ before achieving charge equilibrium is subtracted to eliminate the effect of charge exchange. The influence of charge capture on electron excitation can be seen in Fig. S5 of the Supplemental Material [40]. We take $p(\varepsilon) = \Delta P(\varepsilon)/\Delta t$ to study the velocity dependence of $P(\varepsilon)$, where Δt presents the time spent by the projectiles from achieving charge equilibrium to the final step of the TDDFT simulation.

Figure 2 shows the $p(\varepsilon)$ at various projectile velocities ranging from $v = 0.05$ to 0.20 a.u. in steps of 0.05 a.u. Based on the behavior of $p(\varepsilon)$, we divided the energy range into two regions using dotted and dashed lines. The region below the dotted line is labeled as region II, while the portion between the dotted and dashed lines is denoted as region I. The total number of holes in regions I and II, denoted as $n_{\rm I}$ and $n_{\rm II}$, respectively, is determined by integrating the $p(\varepsilon)$ within these regions. It is evident that the number of excited electrons in region II increases more rapidly with velocity compared to region I. A notable difference between protons and helium ions is observed when their velocities are set to 0.05 a.u. At this velocity, protons fail to excite electrons in region II, whereas helium ions do. However, as the velocity increases to 0.10 a.u., both protons and helium ions are capable of exciting electrons in region II. This discrepancy may explain the presence of a kink velocity in the electronic stopping power of protons, unlike helium ions. Moreover, the proportion $n_{\rm II}/n_{\rm I}$ is 0.03, 0.44, 0.73, and 1.32 for proton projectiles at velocities of 0.05, 0.10, 0.15, and 0.20 a.u., respectively, while it is 0.19, 0.48, 1.15, and 1.60 for helium ions. This suggests that a helium ion possess a stronger ability to excite deep electrons. However, it is important to note that this conclusion is limited to the current simulation environment, i.e., low-energy initially fully bare projectiles moving along the [001] channel with the maximum impact parameter.

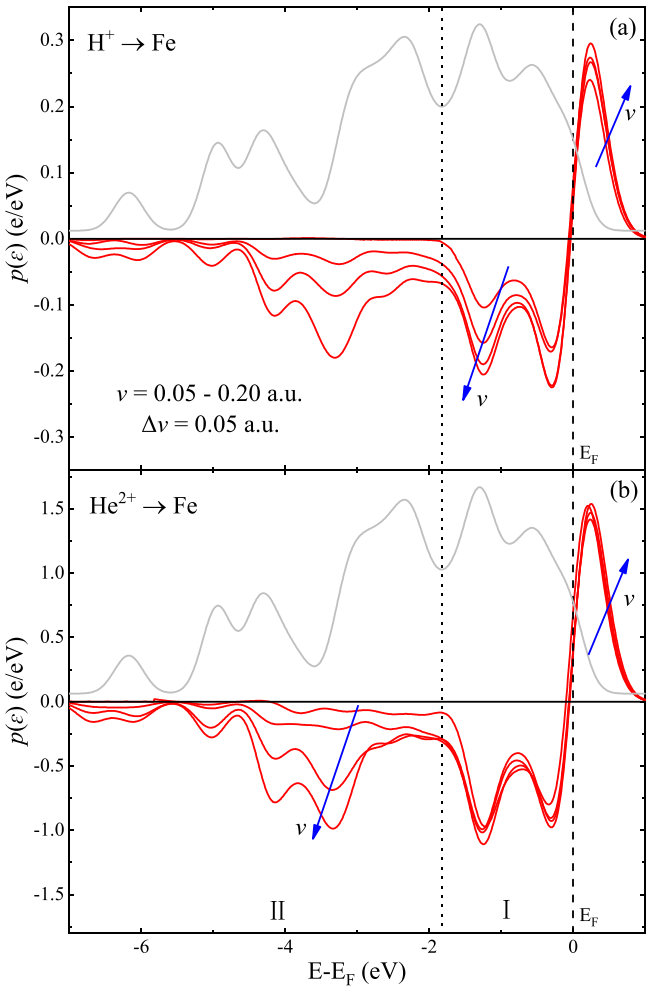

FIG. 2. The averaged excitation distribution $p(\varepsilon)$ for (a) protons and (b) helium ions traveling in Fe under channeling trajectory, for velocities between $v = 0.05$ and 0.20 a.u. in steps of $\Delta v = 0.05$ a.u. The populations of holes and excited electrons, $P(\varepsilon)$, before achieving charge equilibrium is subtracted to eliminate the effect of charge exchange. As the number of electron excitations is proportional to the time t, $p(\varepsilon) = \Delta P(\varepsilon)/\Delta t$ is taken to study the velocity dependence of $P(\varepsilon)$, where Δt presents the time spent by the projectiles from achieving charge equilibrium to the final step of the TDDFT simulation. The gray curves are the electronic density of states, and the scale is different from $p(\varepsilon)$. Gaussian broadening $\sigma = 0.1$ eV.

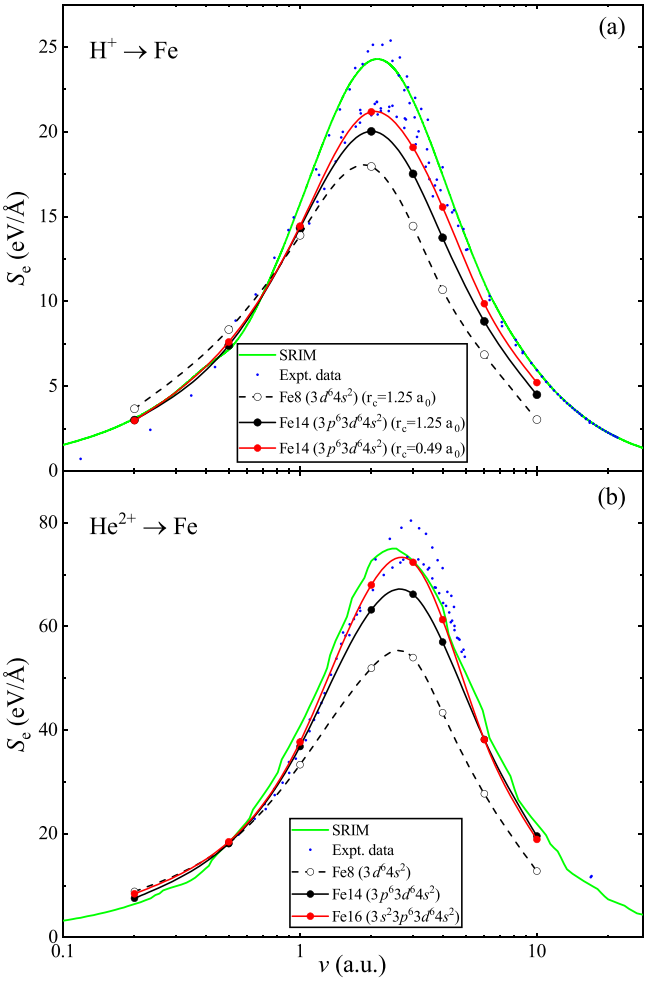

FIG. 3. Electronic stopping power as a function of the velocity for (a) protons and (b) helium ions projectiles under off-channeling trajectories in Fe. Green solid lines result from SRIM [42] and blue dots from the IAEA experimental database [41]. The RT-TDDFT calculated results: (a) Open black circles represent the simulated results of Fe8 and the solid circles represent Fe14. The solid red and black circles present the cutoff radius of the 1s orbital of the hydrogen pseudopotential, which is 0.49 and 1.25 a_0, respectively, and a_0 is the Bohr radius. (b) Open black, solid black, and red circles indicate our simulation results for Fe8, Fe14, and Fe16, respectively. The lines are guides to the eye.

B. The off-channeling stopping

In RT-TDDFT calculations, the S_e for a particular material and projectile ion is mainly influenced by factors such as ion velocity, incidence geometry, and inner-electron excitation [43]. In experiments, the velocity direction of projectiles within the material is uncontrolled, approximating to the off-channeling incidence geometry in simulation calculations, thereby allowing for direct comparison between the calculated off-channeling S_e and experimental data. Figure 3 demonstrates the off-channeling S_e values for protons and helium ions in various valence-electron configurations of host atoms, along with the experimental data [41] and SRIM predictions [42]. Figure 3(a) presents the results for protons. The contribution of the inner 3p electrons of Fe to S_e is determined by comparing the results obtained from two pseudopotentials, Fe8 and Fe14 ($r_c = 1.25\ a_0$, r_c is the cutoff radius of the 1s orbital of protons). The calculated S_e values for Fe8 are higher than the experimental data and SRIM predictions below 1.0 a.u., but are significantly underestimated beyond 1.0 a.u. (by approximately 50% at 10.0 a.u.). The S_e values obtained from Fe14 and SRIM show excellent agreement in the low-velocity regime. However, as the velocity exceeds 0.5 a.u., a noticeable difference arises between them, resulting in an underestimation of the experimental data and SRIM predictions by approximately 25% at 10.0 a.u. The role of 3p electrons in ion dynamics manifests in two ways: (i) They correct the overestimated S_e in the low-velocity regime, which is commonly known as the "shake-up" effect [44], and

(ii) they provide additional channels for electronic energy loss at higher velocities.

After incorporating the effects of the $3p$ electrons, the calculated S_e still remains underestimated beyond the Bragg peak. To further investigate the contribution of the $3s$ electrons, the Fe16 pseudopotential is employed at a velocity of 2.0 a.u. However, this does not yield an improvement in the obtained S_e. Considering that a proton is a light ion and it is challenging to excite the deep-lying electrons of the medium, another proton pseudopotential is constructed by reducing the cutoff radius of the $1s$ orbital from 1.25 to 0.49 a_0. This modification increases the interaction potential between the proton and target at close distances, resulting in a more pronounced excitation of the inner electrons of host atoms. As depicted in Fig. 3(a), the modification of the cutoff radius only affects the high-velocity region (above the Bragg peak). Nevertheless, the results exhibit a more satisfactory agreement with the experimental data. This quantitative agreement strengthens our subsequent discussion of other physical problems and makes it more persuasive. This adjustment of the cutoff radius effectively improves S_e at the Bragg peak and higher velocities, resulting in an increase of approximately 16% in S_e at 10.0 a.u.

Figure 3(b) illustrates the S_e of helium ions. The calculated results obtained from three pseudopotentials exhibit good agreement with the experimental data in the low-velocity regime. However, the S_e of Fe8 deviates from the reference values at 0.5 a.u., and it is severely underestimated by about 40% at 10 a.u. In the case of Fe14, the quantitative difference between the simulated and experimental values becomes increasingly pronounced beyond 1.0 a.u., but this difference diminishes beyond the Bragg peak. The excitation of $3p$ electrons significantly improves the S_e in the middle- and high-velocity regimes, with an increase of about 50% at 10.0 a.u., similar to the case of protons. For the Fe16 model, the S_e agrees well with the experimental results below the Bragg peak. Surprisingly, the difference in S_e between the Fe14 and Fe16 pseudopotentials is only observed around the Bragg peak, suggesting that the $3s$ electrons play an important role in this velocity region. In conclusion, the excitation of inner-shell electrons of Fe exhibits different behavior for protons and helium ions. Helium ions, compared to protons, can excite $3p$ electrons at a much lower velocity (1.0 a.u. for helium ions versus 2.0 a.u. for protons). Additionally, helium ions can significantly excite $3s$ electrons near the Bragg peak, whereas protons cannot. According to the classical pulse approximation, the momentum transferred to a stationary charged particle by a fast ion with charge Z_1 and velocity v is proportional to Z_1/v. Helium ions transfer more momentum than protons at the same velocity, enabling them to excite $3p$ electrons at lower velocities. While the pulse approximation is typically applicable at high velocities, our simulations indicate its validity in explaining the response of inner-shell electrons to ion irradiation, even at velocities as low as approximately 1.0 a.u.

C. Charge state of projectiles

The charge state of ions within materials is a crucial physical quantity in understanding the interaction of ions with matter [45–47], while it is challenging to measure this directly. First-principles simulations provide an opportunity to investigate the charge state of ions in bulk materials. There are generally two methods used to determine the charge state of ions in materials. The first method involves manipulating the Kohn-Sham (KS) orbitals [48–56], such as projecting the Kohn-Sham orbitals onto atomic orbitals. However, this method relies on noninteracting single-particle Kohn-Sham orbitals and lacks rigorous physical interpretation. The second method is based on integrating the electron density around the projectile ions. This method requires the definition of a boundary to differentiate between electrons captured by the ions and those belonging to the target atomic system [57,58]. Typically, this boundary is defined artificially, which may lead to the inclusion of bound electrons from the host atoms in the captured electrons. Therefore, instead of attempting to obtain an exact charge state, it is more informative to focus on the orbital distribution of the charges of projectiles as it can provide a deeper understanding of charge capture behavior. Kononov *et al.* [31] proposed a method to fit the radial distribution of the charges captured by protons using a linear combination of radial distributions of analytic hydrogen orbitals and background electron density. We extend this method to apply it to projectile ions moving within materials.

Figure 4 illustrates the electron density along a line that intersects the proton in both the x- and y-axis directions at a specific moment while the proton is moving within Fe. The figure shows that the moving proton, which attracts electrons, does not significantly disrupt the surrounding electron density. Consequently, the electron density around the projectile ion can be divided into two components: one attracted by the projectile ion (depicted as gray areas in Fig. 4) and the other originating from the target system. The charge state of the projectiles depends on the attracted electrons, and the electron density of the target system can be considered as the background. Here, the term "attracted" was employed to describe the phenomenon that electrons captured by the projectiles undergo polarization within the material. In accordance with the method described in Ref. [31], the radial distribution of the attracted electrons can be expressed as a linear combination of the radial distribution of isolated projectile orbitals using least-squares fits. To more accurately decompose the attracted electrons into the occupation of the projectile's orbital, a spherical region (bounded by the vertical dashed lines in Fig. 4) is defined as the boundary, and its diameter is determined based on the lowest electron density between the projectile and host atoms.

The radial distribution $n(r,t)$ of the attracted electrons, in units of e/a_0, can be expressed as

$$n(r,t) = \frac{1}{\Delta r}\int_{S[r,\mathbf{R}(t)]} dr^3[n(\mathbf{r},t) - n(\mathbf{r},t_0)], \tag{4}$$

where the $S[r,\mathbf{R}(t)]$ is the spherical shell of thickness Δr and radius r, centered at the projectile's position $\mathbf{R}$(t). The $n(\mathbf{r},t)$ and the $n(\mathbf{r},t_0)$ are the electron density of the time-dependent evolution and the original ground state, respectively. The radial distribution $n(r,t)$, integrated again over r, would obtain the total number of electrons that are attracted. The electron density in our simulations is represented by a real-space grid,

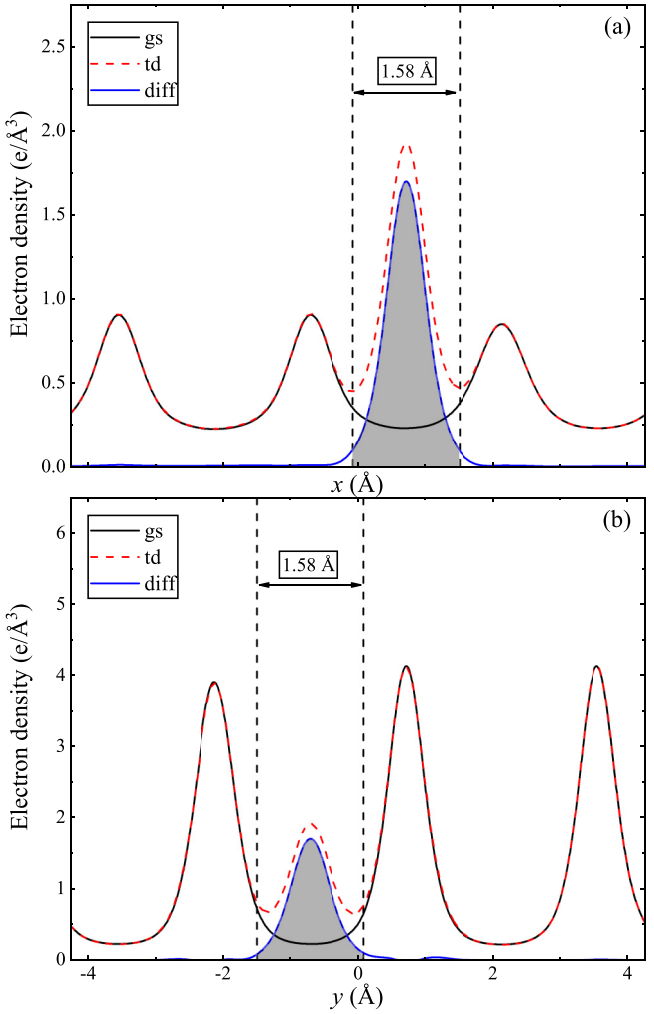

FIG. 4. The electron density on a line crossing the proton along the (a) x and (b) y directions of the simulation cell when the projectile moves on an off-channeling trajectory in Fe at the velocity of 0.2 a.u. The red dashed curves represent the electron density of time-dependent evolution. The black solid curves correspond to the electron density of the ground state on the same line. The blue solid curves indicate their difference. The gray areas are the region where we performed the electron orbital decomposition.

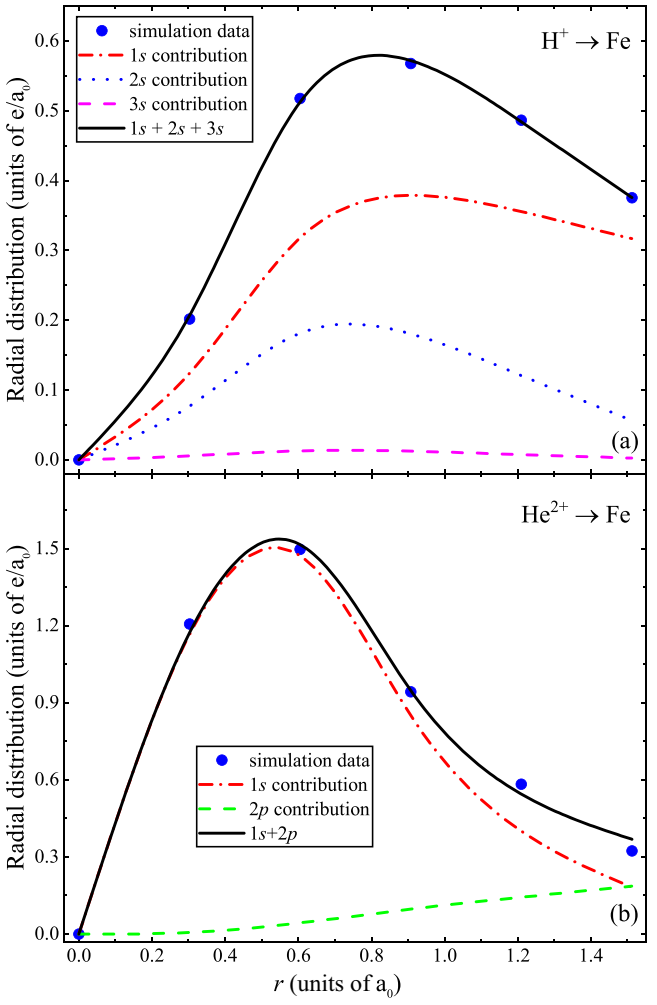

FIG. 5. The solid blue circles show the simulated radial distribution of the electronic density captured by the off-channeling (a) proton and (b) helium ion at the velocity of 0.2 a.u. The least squares are used to fit the simulation results using the radial distribution of ground-state Kohn-Sham orbitals of the isolated proton and helium ion, and the results are shown as curves.

so Eq. (4) can be expressed in a discretized form as

$$n(r_i, t) = \frac{1}{\Delta r} \sum_{r_{i-1} < |\mathbf{r}-\mathbf{R}(t)| \leqslant r_i} [n(\mathbf{r}, t) - n(\mathbf{r}, t_0)]\Delta V, \qquad (5)$$

where $r_i = i\Delta r$ ranges from 0 to 1.5 a_0 and ΔV is the volume of each grid cell. Considering the region defined in Fig. 4, we select Δr to be 0.3 a.u.

We fit the calculated radial distribution of charges attracted by the projectiles to a linear combination of the radial distribution of the ground-state Kohn-Sham orbitals of isolated H^+ and He^{2+}, as shown in Fig. 5. The resulting fits accurately capture the simulated radial distribution, with R^2 values above 0.97 for all our fits. The radial distribution of the ground-state Kohn-Sham orbitals of isolated H^+ and He^{2+} can be found in Fig. S6 of the Supplemental Material [40]. In Fig. 5, certain orbitals are not included, indicating that these orbitals have no contribution [$2p$, $3p$, and $3d$ orbitals in Fig. 5(a) and $2s$, $3s$, $3p$, and $3d$ orbitals in Fig. 5(b)]. We conducted a more precise test with a spacing of 0.10 Å, and the number of valid simulated data points was increased to seven accordingly, which showed a negligible change, as shown in Fig. S7 of the Supplemental Material [40]. Integrating fitted radial distributions over r, the electron occupations for individual orbitals can be obtained as follows:

$$n_{nl} = \int n_{nl}(r)dr, \qquad (6)$$

where n_{nl} denotes the charges occupying an orbital with the principal quantum number n and the angular quantum number l, and $n_{nl}(r)$ denotes the fitted radial distribution of the charges of the orbital with the principal quantum number n and angular quantum number l.

In Fig. 6(a), we present the charges decomposed into each electron orbital of the proton, as determined by Eq. (6), when the proton follows an off-channeling trajectory at a velocity

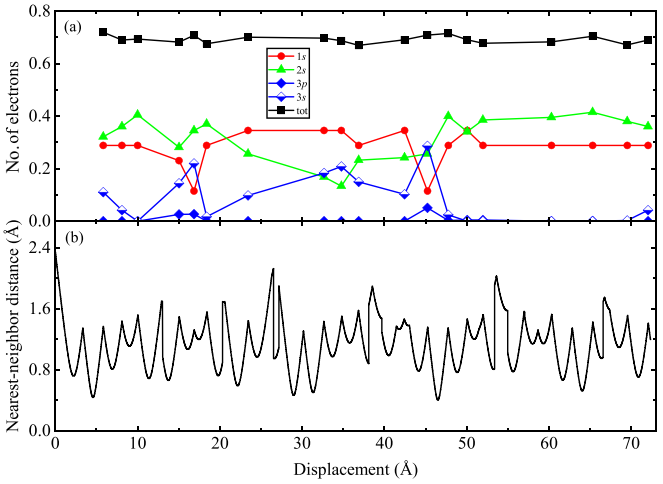

FIG. 6. (a) The electrons attracted by the off-channeling proton, decomposed into the 1*s*, 2*s*, 3*s*. and 3*p* orbitals of hydrogen, as a function of projectile displacement at the velocity of 0.2 a.u. (b) First-nearest-neighbor (NN) distance between the proton and host atoms as a function of proton displacement.

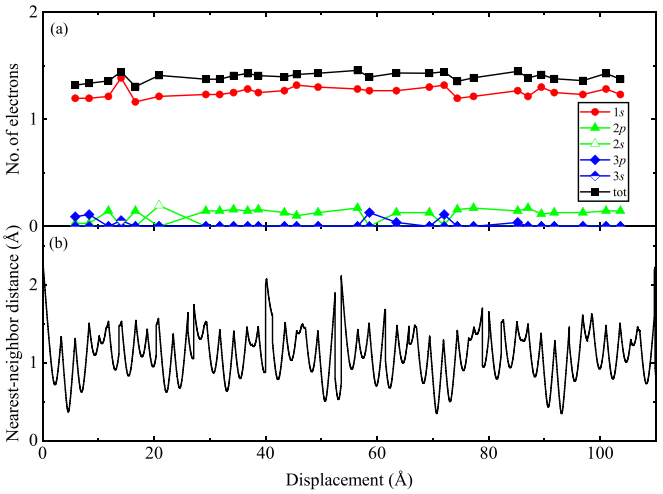

FIG. 7. (a) The electrons attracted by the off-channeling helium ion, decomposed into the 1*s*, 2*s*, 2*p*, 3*s*, and 3*p* orbitals of helium, as a function of projectile displacement at 0.2 a.u. velocity. (b) First-nearest-neighbor (NN) distance between the helium ion and host atoms as a function of the helium ion's displacement.

of 0.2 a.u. Figure 6(b) illustrates the distance between the proton and the first-nearest-neighbor host atom. The orbital decomposition is performed where the target electron density is locally minimal, ensuring that the influence of the surrounding host atoms on the attracted electrons is minimal. The results reveal that the electrons attracted by the off-channeling proton primarily occupy the 1*s*, 2*s*, and 3*s* orbitals. The occupations of these orbitals exhibit significant fluctuations as the proton moves and stabilize after the proton has traveled approximately 50 Å. Conversely, the total charges fluctuate only slightly, indicating that the attracted charges continually adjust their orbital distribution during motion until reaching equilibrium. This observation suggests that the electrons attracted by protons are sensitive to changes in the environment, possibly indicating a polarization effect. For high-velocity protons, the occupations in different orbitals oscillate more vigorously and continue oscillating until the end of the simulation, as demonstrated in Fig. S8 of the Supplemental Material [40]. This behavior may be attributed to the small energy interval between related atomic orbitals in hydrogen, resulting in frequent electron transitions. The electrons attracted by off-channeling protons at 1.0 a.u. amount to approximately 0.65, which is consistent with the result for protons in Al [31]. In comparison to protons escaping from materials, the electrons that are attracted by protons within materials occupy higher-n orbitals. The former predominantly occupy the $n = 1$ orbital [31], while the latter are also distributed in the $n = 2$ and 3 orbitals at low velocities.

For the off-channeling helium ion at 0.2 a.u., as displayed in Fig. 7(a), the majority of attracted electrons occupy the 1*s* orbital of helium ions. The remaining electrons are mainly found in the 2*p* and 3*p* orbitals, with occasional occupation of the 2*s* and 3*s* orbitals during the motion of the projectile. Unlike protons, the electrons in the 1*s* orbital of helium ions are not significantly excited to other orbitals as the ions move. This can be attributed to the larger energy separation between related atomic orbitals of helium ions compared to protons, making electron transition less likely to occur. However, a few electrons may still transition between high-n orbitals during the projectile's motion, possibly due to polarization effects. At 1.0 a.u., the occupations in high-n orbitals display a noticeable increase, but primarily concentrate in the 1*s* orbital, as demonstrated in Fig. S9 of the Supplemental Material [40].

The charge decomposition is also conducted for channeling projectiles at 0.2 a.u., as shown in Fig. 8. In the case of the channeling proton [Fig. 8(a)], the electrons in the 1*s* and 2*s* orbitals are more stable. The total charges attracted by the channeling proton remain the same as the off-channeling case, as shown in Fig. 6(a), at approximately 0.7. For the channeling helium ion [Fig. 8(b)], the total charges attracted amount to around 0.8, with approximately 0.6 in the 1*s* orbital and the remaining charges randomly occupying high-n orbitals. Conversely, the total charges attracted by the off-channeling helium ion at 0.2 a.u. are about 1.4 [as seen in Fig. 7(a)], with approximately 1.3 in the 1*s* orbital and 0.1 in other orbitals. This indicates that the total charges attracted by helium ions depend on the trajectory of the ions. It is noteworthy that for channeling projectiles at 0.2 a.u., the absolute charges are 0.3 for protons and 1.2 for helium ions. The difference in absolute charges is likely the direct reason why low-energy channeling helium ions can excite deeper electrons. In summary, the orbital distribution of electrons attracted by protons is sensitive to the trajectories of the projectile ions, and the trajectories of helium ions significantly influence the occupations of attracted electrons in the 1*s* orbital of helium ions (approximately 0.6 electrons in the 1*s* orbital for the channeling trajectory and approximately 1.3 electrons in the 1*s* orbital for the off-channeling trajectory at 0.2 a.u.).

IV. CONCLUSIONS

In this study, we simulated the electron-ion excitation dynamics of protons and helium ions in Fe using first

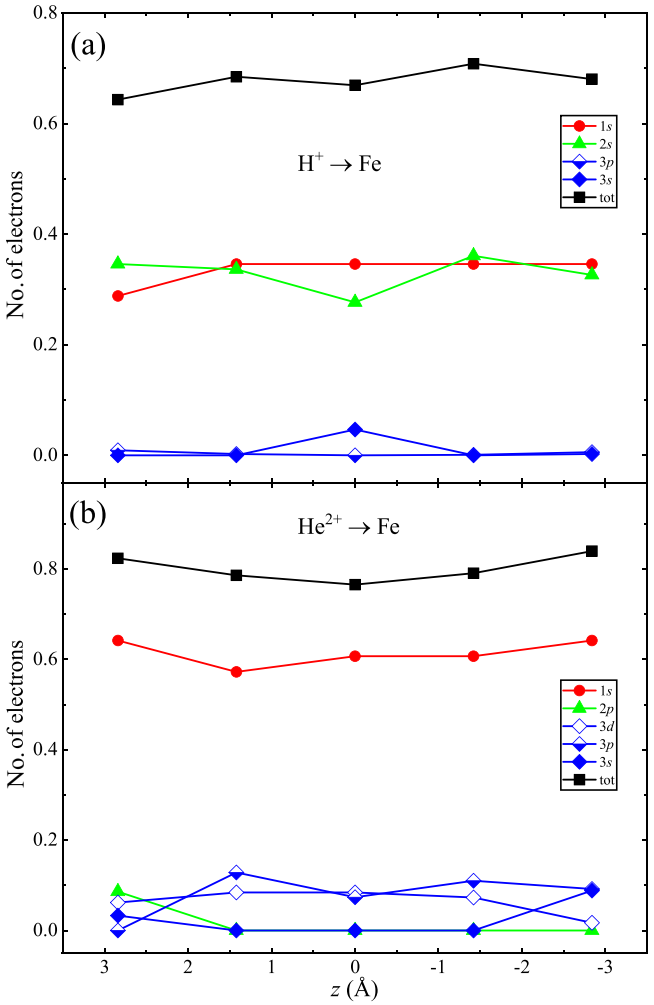

FIG. 8. The electrons attracted by (a) channeling protons and (b) helium ions, decomposed into the orbitals of $n = 1$, 2, and 3 of projectiles, as a function of z coordinates at 0.2 a.u. velocity. Solid black squares indicate the electrons attracted by proton and helium ion projectiles. The colored symbols indicate the electrons in the individual orbitals of the projectile. All data are obtained where the projectiles are farthest from the target atoms.

principles based on real-time time-dependent density functional theory. Our investigations have three main focuses. First, the electronic stopping power of Fe is investigated when the projectiles traverse along the channeling trajectory at low velocities. Notably, the channeling S_e of protons exhibited a deviation from the velocity proportionality, a characteristic not observed for helium ions. This disparity is attributed to the stronger excitation power of helium ions, enabling them to excite deeper d electrons at lower velocities.

Second, the off-channeling S_e is calculated in a wide range of velocities. The computed S_e, accounting for inner-electron excitation, aligned well with the experimental data up to the Bragg peak. Furthermore, the use of different pseudopotentials yielded fresh insights into understanding core electron excitation. Specifically, the $3p$ electrons of Fe significantly contribute to the S_e in the middle- and high-velocity regimes for both protons and helium ions. Additionally, a quantitative description of the stopping maximum for helium ions necessitated the inclusion of $3s$ electrons. In a word, the electrons of Fe with $n \geqslant 3$ dominate the electronic stopping power of protons and helium ions in Fe in a wide range of velocities.

Third, we expanded the electron decomposition method proposed in Ref. [31] and applied it to the projectiles moving in Fe. For the off-channeling projectile at 0.2 a.u., the charges attracted by the proton primarily occupy the $1s$, $2s$, and $3s$ orbitals, with unstable occupations in each orbital during projectile motion. In contrast, the charges attracted by the helium ion predominantly and stably occupy the $1s$ orbital. For the low-velocity channeling projectiles, the occupations of protons in each orbital remained stable, with the attracted electrons mainly occupying the $1s$ and $2s$ orbitals. However, the channeling helium ion attracts fewer $1s$ electrons, i.e., approximately half of those attracted by the off-channeling helium ion.

This work examined the electronic stopping power in detail for protons and helium ions in Fe, and the electrons attracted by the projectiles moving in Fe are decomposed into the occupation of projectile orbitals. Insights are provided to understand the electron excitation and charge transfer.

ACKNOWLEDGMENTS

This work was financially supported by the National MCF Energy R&D Program of China (Grant No. 2022YFE03110000) and National Natural Science Foundation of China (Grant No. 11975119).

[1] E. Rutherford, Philos. Mag. **21**, 669 (1911).
[2] G. Odette and B. D. Wirth, in *Handbook of Materials Modeling*, edited by S. Yip (Springer, Netherlands, 2005), pp. 999–1037.
[3] G. S. Was, *Fundamentals of Radiation Materials Science* (Springer, Berlin, 2007).
[4] I. Monnet, C. Grygiel, M. L. Lescoat, and J. Ribis, J. Nucl. Mater. **424**, 12 (2012).
[5] A. C. Begg, F. A. Stewart, and C. Vens, Nat. Rev. Cancer **11**, 239 (2011).
[6] A. Vantomme, Nucl. Instrum. Methods Phys. Res. Sect. B **371**, 12 (2016).
[7] S. Limandri, P. de Vera, R. C. Fadanelli, L. C. C. M. Nagamine, A. Mello, R. Garcia-Molina, M. Behar, and I. Abril, Phys. Rev. E **89**, 022703 (2014).
[8] P. D. Townsend, P. J. Chandler, and L. Zhang, *Optical Effects of Ion Implantation* (Cambridge University Press, Cambridge, 1994).
[9] S. Duzellier, Aerosp. Sci. Technol. **9**, 93 (2005).
[10] *Ionizing Radiation Effects in Electronics: From Memories to Imagers*, edited by M. Bagatin and S. Gerardin (CRC Press, Taylor and Francis, Boca Raton, 2015).
[11] H. Bethe, Ann. Phys. **397**, 325 (1930).
[12] A. A. Correa, Comput. Mater. Sci. **150**, 291 (2018).

[13] G. Martínez-Tamayo, J. C. Eckardt, G. H. Lantschner, and N. R. Arista, Phys. Rev. A **54**, 3131 (1996).
[14] D. Primetzhofer, S. Rund, D. Roth, D. Goebl, and P. Bauer, Phys. Rev. Lett. **107**, 163201 (2011).
[15] E. Fermi and E. Teller, Phys. Rev. **72**, 399 (1947).
[16] P. M. Echenique, R. M. Nieminen, and R. H. Ritchie, Solid State Commun. **37**, 779 (1981).
[17] D. Goebl, D. Roth, and P. Bauer, Phys. Rev. A **87**, 062903 (2013).
[18] D. Goebl, W. Roessler, D. Roth, and P. Bauer, Phys. Rev. A **90**, 042706 (2014).
[19] J. E. Valdés, J. C. Eckardt, G. H. Lantschner, and N. R. Arista, Phys. Rev. A **49**, 1083 (1994).
[20] S. N. Markin, D. Primetzhofer, S. Prusa, M. Brunmayr, G. Kowarik, F. Aumayr, and P. Bauer, Phys. Rev. B **78**, 195122 (2008).
[21] M. A. Sortica, V. Paneta, B. Bruckner, S. Lohmann, M. Hans, T. Nyberg, P. Bauer, and D. Primetzhofer, Phys. Rev. A **96**, 032703 (2017).
[22] D. Roth, B. Bruckner, M. V. Moro, S. Gruber, D. Goebl, J. I. Juaristi, M. Alducin, R. Steinberger, J. Duchoslav, D. Primetzhofer, and P. Bauer, Phys. Rev. Lett. **118**, 103401 (2017).
[23] C. P. Race, D. R. Mason, M. W. Finnis, W. M. C. Foulkes, A. P. Horssfield, and A. P. Sutton, Rep. Prog. Phys. **73**, 116501 (2010).
[24] P. Sigmund and A. Schinner, Eur. Phys. J. D **68**, 318 (2014).
[25] J. F. Ziegler, J. Appl. Phys. **85**, 1249 (1999).
[26] W. Q. Jin, F. Mao, S. M. Li, W. Q. Zuo, R. D. Chen, G. G. Xiong, H. Mao, F. Wang, and F. S. Zhang, Phys. Chem. Chem. Phys. **25**, 9043 (2023).
[27] D. C. Yost, Y. Yao, and Y. Kanai, Phys. Rev. B **96**, 115134 (2017).
[28] A. Schleife, Y. Kanai, and A. A. Correa, Phys. Rev. B **91**, 014306 (2015).
[29] E. E. Quashie and A. A. Correa, Phys. Rev. B **98**, 235122 (2018).
[30] Y. Yao, D. C. Yost, and Y. Kanai, Phys. Rev. Lett. **123**, 066401 (2019).
[31] A. Kononov and A. Schleife, Phys. Rev. B **102**, 165401 (2020).
[32] E. Runge and E. K. U. Gross, Phys. Rev. Lett. **52**, 997 (1984).
[33] M. A. L. Marques and E. K. U. Gross, Annu. Rev. Phys. Chem. **55**, 427 (2004).
[34] C. A. Ullrich and Z.-H. Yang, Braz. J. Phys. **44**, 154 (2014).
[35] X. Andrade, J. Alberdi-Rodriguez, D. A. Strubbe, M. J. T. Oliveira, F. Nogueira, A. Castro, J. Muguerza, A. Arruabarrena, S. G. Louie, A. Aspuru-Guzik, A. Rubio, and M. A. L. Marques, J. Phys.: Condens. Matter **24**, 233202 (2012).
[36] X. Andrade, D. A. Strubbe, U. De Giovannini, A. H. Larsen, M. J. T. Oliveira, J. Alberdi-Rodriguez, A. Varas, I. Theophilou, N. Helbig, M. Verstraete, L. Stella, F. Nogueira, A. Aspuru-Guzik, A. Castro, M. A. L. Marques, and A. Rubio, Phys. Chem. Chem. Phys. **17**, 31371 (2015).
[37] N. Troullier and J. L. Martins, Phys. Rev. B **43**, 1993 (1991).
[38] J. P. Perdew and Y. Wang, Phys. Rev. B **45**, 13244 (1992).
[39] A. Castro, M. A. L. Marques, and A. Rubio, J. Chem. Phys. **121**, 3425 (2004).
[40] See Supplemental Material at http://link.aps.org/supplemental/10.1103/PhysRevA.109.032807 for details regarding the electronic stopping power, additional results for electronic stopping power, the electronic densities of states for transition metals, details regarding the occupation of holes and excited electrons, and additional results for electron captured.
[41] International atomic energy agency nuclear data services, stopping power of matter for ions: Hydrogen and helium ions, https://www-nds.iaea.org/stopping (unpublished).
[42] J. F. Ziegler, M. D. Ziegler, and J. P. Biersack, Nucl. Instrum. Methods Phys. Res. Sect. B **268**, 1818 (2010).
[43] J. Halliday and E. Artacho, Phys. Rev. B **100**, 104112 (2019).
[44] P. Persson, S. Lunell, A. Szöke, B. Ziaja, and J. Hajdu, Protein Sci. **10**, 2480 (2001).
[45] K. G. Reeves, Y. Yao, and Y. Kanai, Phys. Rev. B **94**, 041108(R) (2016).
[46] J. Lindhard, K. Dan. Vidensk. Selsk. Mat. Fys. Medd. **28**, 1 (1954).
[47] J. Lindhard and A. Winther, K. Dan. Vidensk. Selsk. Mat. Fys. Medd. **34**, 1 (1964).
[48] R. S. Mulliken, J. Chem. Phys. **23**, 1833 (1955).
[49] P. G. Reinhard and E. Suraud, J. Cluster Sci. **10**, 239 (1999).
[50] O. Knospe, J. Jellinek, U. Saalmann, and R. Schmidt, Eur. Phys. J. D **5**, 1 (1999).
[51] C. M. Isborn, X. Li, and J. C. Tully, J. Chem. Phys. **126**, 134307 (2007).
[52] J. M. Pruneda, D. Sánchez-Portal, A. Arnau, J. I. Juaristi, and E. Artacho, Phys. Rev. Lett. **99**, 235501 (2007).
[53] Y. Miyamoto and H. Zhang, Phys. Rev. B **77**, 161402(R) (2008).
[54] F. Wang, X. C. Xu, X. H. Hong, J. Wang, and B. C. Gou, Phys. Lett. A **375**, 3290 (2011).
[55] F. Wang, X. H. Hong, J. Wang, B. C. Gou, and J. G. Wang, Phys. Lett. A **376**, 469 (2012).
[56] C.-Z. Gao, J. Wang, and F.-S. Zhang, Chem. Phys. **410**, 9 (2013).
[57] T. A. Manz and N. G. Limas, RSC Adv. **6**, 47771 (2016).
[58] N. G. Limas and T. A. Manz, RSC Adv. **6**, 45727 (2016).